



ORIGINAL ARTICLE OPEN ACCESS

Myo-Guide: A Machine Learning-Based Web Application for Neuromuscular Disease Diagnosis With MRI

Jose Verdu-Diaz¹  | Carla Bolano-Díaz¹ | Alejandro Gonzalez-Chamorro¹ | Sam Fitzsimmons¹ | Jodi Warman-Chardon^{2,3} | Goknur Selen Kocak¹ | Debora Mucida-Alvim¹ | Ian C. Smith⁴ | John Vissing⁵ | Nanna Scharff Poulsen⁵ | Sushan Luo⁶ | Cristina Domínguez-González⁷ | Laura Bermejo-Guerrero⁷ | David Gomez-Andres⁸ | Javier Sotoca⁹ | Anna Pichiecchio^{10,11} | Silvia Nicolosi¹² | Mauro Monforte¹³ | Claudia Brogna¹⁴ | Eugenio Mercuri¹⁵ | Jorge Alfredo Bevilacqua¹⁶ | Jorge Díaz-Jara¹⁶ | Benjamín Pizarro-Galleguillos¹⁷ | Peter Krkoska¹⁸ | Jorge Alonso-Pérez¹⁹ | Montse Olivé^{20,21,22} | Erik H. Niks²³ | Hermien E. Kan²⁴ | James Lilleker²⁵ | Mark Roberts²⁵ | Bianca Buchignani²⁶ | Jinhong Shin²⁷ | Florence Esselin²⁸ | Emmanuelle Le Bars²⁹ | Anne Marie Childs³⁰ | Edoardo Malfatti³¹ | Anna Sarkozy³² | Luke Perry³² | Sniya Sudhakar³³ | Edmar Zanoteli³⁴ | Filipe Tupinamba Di Pace³⁴ | Emma Matthews³⁵ | Shahram Attarian³⁶ | David Bendahan³⁷ | Matteo Garibaldi³⁸ | Laura Fionda³⁹ | Alicia Alonso-Jiménez⁴⁰ | Robert Carlier⁴¹ | Ali Asghar Okhovat⁴² | Shahriar Nafissi⁴² | Atchayaram Nalini⁴³ | Seena Vengalil⁴³ | Kieren Hollingsworth⁴⁴ | Chiara Marini-Bettolo¹ | Volker Straub¹ | Giorgio Tasca¹ | Jaume Bacardit⁴⁵ | Jordi Díaz-Manera¹  | the Myo-Guide Consortium

Correspondence: Jordi Díaz-Manera (jordi.diaz-manera@newcastle.ac.uk)

Received: 18 September 2024 | **Revised:** 14 February 2025 | **Accepted:** 25 March 2025

Funding: Jose Verdu-Diaz, Carla Bolano-Díaz, Alejandro Gonzalez-Chamorro, Sam Fitzsimmons, Jaume Bacardit and Jordi Díaz-Manera disclose support for the research of this work from Muscular Dystrophy UK (grant number: 22GRO-PG24-0575 and 24GRO-PG24-0736-1) and AFM-Telethon (grant number: 23444). Jose Verdu-Diaz is also supported by the NHIR Newcastle Biomedical Research Centre (BRC) (grant number: NIHR203309). The NHIR Newcastle BRC is a partnership between Newcastle Hospitals NHS Foundation Trust and Newcastle University, funded by the National Institute for Health and Care Research (NIHR). The views expressed are those of the authors and not necessarily those of the NIHR or the Department of Health and Social Care.

Keywords: artificial intelligence | differential diagnosis | machine learning | MRI | neuromuscular diseases

ABSTRACT

Background: Neuromuscular diseases (NMDs) are rare disorders characterized by progressive muscle fibre loss, leading to replacement by fibrotic and fatty tissue, muscle weakness and disability. Early diagnosis is critical for therapeutic decisions, care planning and genetic counselling. Muscle magnetic resonance imaging (MRI) has emerged as a valuable diagnostic tool by identifying characteristic patterns of muscle involvement. However, the increasing complexity of these patterns complicates their interpretation, limiting their clinical utility. Additionally, multi-study data aggregation introduces heterogeneity challenges. This study presents a novel multi-study harmonization pipeline for muscle MRI and an AI-driven diagnostic tool to assist clinicians in identifying disease-specific muscle involvement patterns.

Methods: We developed a preprocessing pipeline to standardize MRI fat content across datasets, minimizing source bias. An ensemble of XGBoost models was trained to classify patients based on intramuscular fat replacement, age at MRI and sex. The SHapley Additive exPlanations (SHAP) framework was adapted to analyse model predictions and identify disease-specific muscle involvement patterns. To address class imbalance, training and evaluation were conducted using class-balanced metrics. The model's performance was compared against four expert clinicians using 14 previously unseen MRI scans.

Results: Using our harmonization approach, we curated a dataset of 2961 MRI samples from genetically confirmed cases of 20 paediatric and adult NMDs. The model achieved a balanced accuracy of $64.8\% \pm 3.4\%$, with a weighted top-3 accuracy of $84.7\% \pm 1.8\%$ and top-5 accuracy of $90.2\% \pm 2.4\%$. It also identified key features relevant for differential diagnosis, aiding clinical

For affiliations refer to page 13.

This is an open access article under the terms of the [Creative Commons Attribution](https://creativecommons.org/licenses/by/4.0/) License, which permits use, distribution and reproduction in any medium, provided the original work is properly cited.

© 2025 The Author(s). *Journal of Cachexia, Sarcopenia and Muscle* published by Wiley Periodicals LLC.

decision-making. Compared to four expert clinicians, the model obtained the highest top-3 accuracy ($75.0\% \pm 4.8\%$). The diagnostic tool has been implemented as a free web platform, providing global access to the medical community.

Conclusions: The application of AI in muscle MRI for NMD diagnosis remains underexplored due to data scarcity. This study introduces a framework for dataset harmonization, enabling advanced computational techniques. Our findings demonstrate the potential of AI-based approaches to enhance differential diagnosis by identifying disease-specific muscle involvement patterns. The developed tool surpasses expert performance in diagnostic ranking and is accessible to clinicians worldwide via the Myo-Guide online platform.

1 | Introduction

Neuromuscular diseases (NMDs) are a heterogeneous group of disorders affecting the function of skeletal muscle, often characterized by progressive muscle wasting and its substitution by non-contractile fatty and connective tissue. NMDs can manifest across all age groups and are associated with a wide range of clinical presentations, from mild muscle weakness to severe disability, and are sometimes associated with life-threatening complications [1].

An early and accurate diagnosis is a critical step in effectively managing and treating NMDs. However, diagnosing these disorders presents a challenge due to their diverse and overlapping clinical presentations. Magnetic resonance imaging (MRI) has increased in popularity during the last decades as a tool for studying NMDs, as it allows for muscle and fatty tissue differentiation [2, 3].

Different methods exist to assess fat replacement, which can be categorized into two broad groups: quantitative and semi-quantitative. The main quantitative technique for intramuscular fat assessment is the chemical shift-based water and fat separation (or Dixon) technique. This imaging technique separates fat and water signals in different images, allowing the reconstruction of a fat fraction (FF) map [4]. A precise measure of the FF can then be retrieved by selecting regions of interest (ROIs) in the FF map [5]. Although this technique yields a reliable measurement, most of the available retrospective data consist of qualitative T1w scans [2]. The main semi-quantitative techniques are based on the Mercuri score, a visual 5-point scale ranging from 0 (*healthy muscle*) to 4 (*completely fat-replaced muscle*) [6].

Muscle fatty replacement is not random, and different disease-causing genes have been linked to the selective involvement of groups of muscles. This has allowed the identification of the so-called patterns of fat replacement, which are useful in proposing a potential diagnosis [7–9]. However, the number of patterns described has increased considerably, making the identification of patterns a complex and time-consuming task that requires a high degree of expertise. Moreover, many of these patterns are overlapping, and there is no atlas collecting and keeping findings up to date [9]. This complexity is ideally suited for the capability of artificial intelligence (AI) techniques, allowing for a deeper analysis of muscle fat replacement patterns [10].

Emerging AI tools have proven to be useful for the diagnosis of NMDs using MRI data [11–13]. However, current studies

are focused on a relatively small number of NMDs, and the identified patterns lose specificity when compared against a larger pool of disorders [14]. In 2020, we published a paper sharing the results of a pilot machine learning-based (ML) tool for diagnosing multiple NMDs using MRI data [15]. We demonstrated that supervised ML techniques are useful for NMD diagnosis, and we also identified several limitations that require addressing:

- AI models are often considered hard-to-interpret black boxes. However, in clinical settings, model explainability is critical to validate the results of such models. Furthermore, understanding the decision process of a diagnosis model can help identify novel insights about the disease's evolution. Multiple AI explainability techniques have been presented; however, these are yet to be used and adapted for understanding muscle involvement in NMD patients.
- The impact of AI models for patient diagnostics is limited by their accessibility, and clinicians require an interface to interact with such models.
- Current approaches have targeted a limited number of diseases, and there is a need for a general model, able to generalize over a larger pool of disorders.

Additionally, collecting a dataset eligible for AI analysis demands joining retrospective data from multiple sites and multiple studies, leading to different types of heterogeneity in the data [16]:

- Scale: Intramuscular fat replacement can be measured using multiple continuous and discrete scales. All scales describe a value for healthy and completely fat-replaced muscle; however, discrete scales do not align on how the severity is quantized. Unless the proportion of samples using each scale is equal across NMDs, the degree of muscle involvement may be emphasized more in some conditions than others in the compiled dataset. This effect, known as scale information leakage, may lead to false predictors in diagnosis (Figure 1a).
- Muscle grouping: Researchers often group muscles due to similar function or involvement, spatial proximity or low MRI scan resolution (i.e. grouping the psoas and iliacus muscles into iliopsoas). Integrating data from studies using different feature groups requires a flexible data model able to unify the feature space.
- Bilateral/unilateral scores: Muscle fat replacement can be scored for both sides of the body (left and right) at

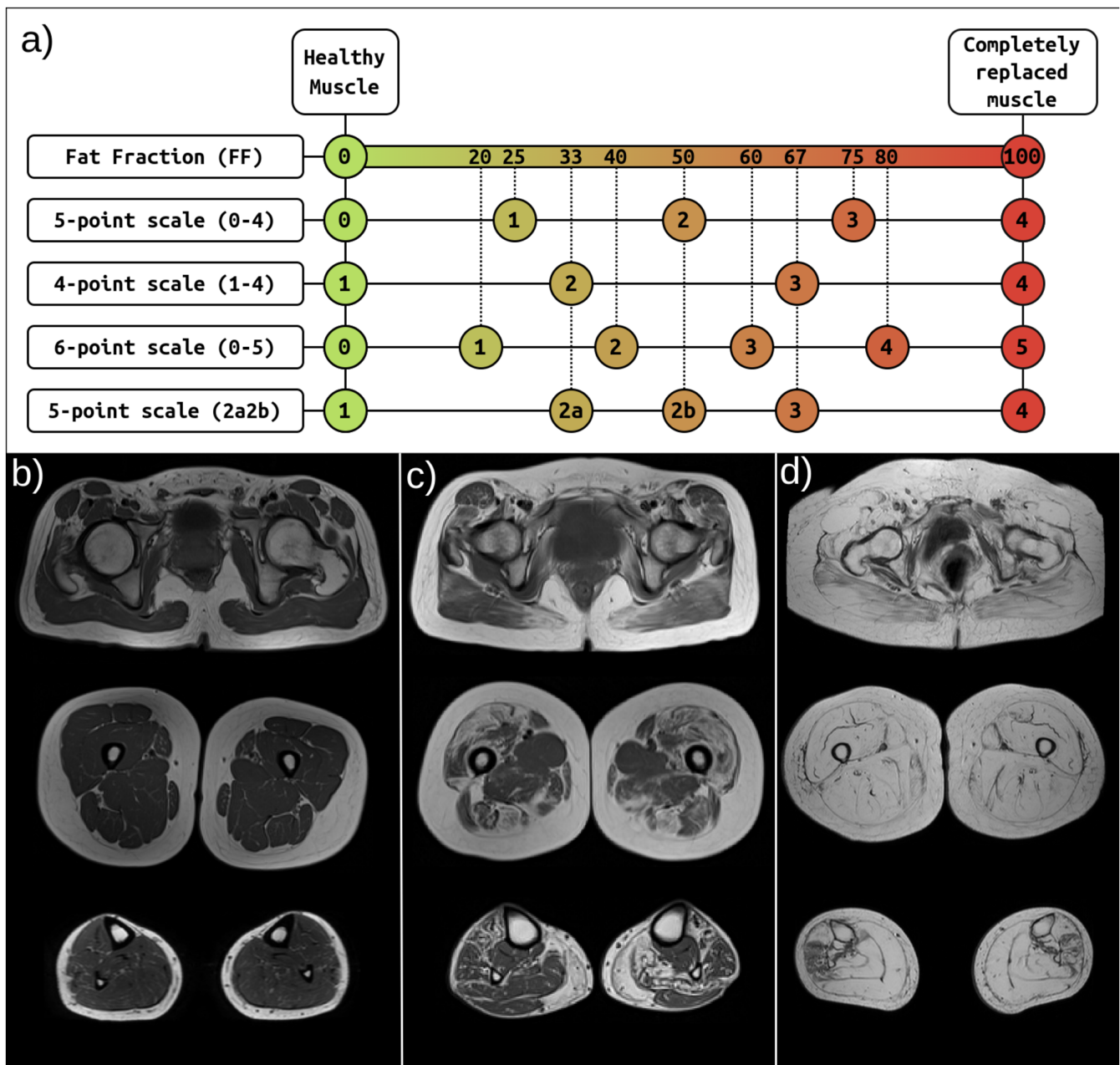


FIGURE 1 | (a) Representation of the different muscle fat scales found in the dataset. Each row represents a different scale, and each coloured circle represents a possible value. The fat fraction scale is continuous, and the rest are discrete. Discrete scales are projected over the FF scale to show differences in muscle fat quantisation. (b) MRI examples of healthy muscle, (c) intermediate-stage muscle and (d) late-stage muscle. Fatty tissue appears with high intensity in the MRIs (white/light grey), whereas muscle tissue appears with low intensity (dark grey). The top row of the MRIs represents a pelvis/waist-level axial slice, the second row represents a thigh axial slice, and the last row represents a calf axial slice.

the expense of increasing the time required for scoring. However, most NMDs show symmetrical muscle involvement, resulting in redundant information when reporting the data. For the sake of time and visual clarity, some researchers choose to report unilateral or average scores.

This heterogeneity can bias classification models if not accounted for. Therefore, a data harmonization pipeline is required to adapt muscle fat replacement measurements to a unique scale.

In this paper, we aim to provide solutions to these limitations. We present the following:

- A software pipeline for multi-study and/or multicentre muscle MRI data harmonization.
- The collection of the largest available multi-study dataset for NMDs, consisting of 3463 patient records across 40 diseases.
- A scalable NMD diagnosis ensemble model based on the XGBoost algorithm.

- An adaptation of current AI explainability methods (SHapley Additive exPlanations [SHAP]) and the creation of novel visualization techniques to identify and understand discriminative patterns of muscle involvement in NMDs.
- Myo-Guide, a web portal hosting the diagnosis model and serving as a platform for pushing forward the role of MRI in the study of NMDs.

2 | Materials and Methods

2.1 | Study Data

We established the Myo-Guide consortium to collect a large MRI data repository on a wide range of NMDs. Thirty-four clinical sites from Europe, America and Asia collaborate by sharing MRI scans and muscle fat data via the secure Myo-Share platform [17]. Published datasets of muscle fat replacement were also incorporated [S1–S24]. Age and sex were collected when available.

All included patients required a confirmed genetic diagnosis. T1-weighted lower limb MRI scans were collected, and all muscles were scored using a 5-point scale (values from 0 to 4) by an experienced clinician. Left and right muscles were scored to assess asymmetric involvement. Already existing muscle fat scores were directly integrated. The number of samples extracted from the literature are as follows: GNE (31), SarcoG (155), PABPN1 (277), FKRP (93), DUX4 (153), LMNA (37), CAPN3 (82), SMN1 (55), OPDM (77), ANO5 (26), DMD (119), DMPK (134) and PYGM (46). All samples of the disorders not mentioned were manually scored by Diaz-Manera J., Bolaño-Diaz C. and Selen Kocak G.

For longitudinal data, each time point was considered a new sample. To avoid data leakage from non-independent samples, we grouped samples by patient and used each group exclusively for training or testing.

As of submission, the Myo-Guide Consortium has gathered 3463 lower limb muscle MRI samples from patients genetically diagnosed with 40 NMDs. We selected all diseases with at least 30 samples, resulting in 2961 samples from 20 NMDs. An overview of this subset and labels used for each disease is available in Table 1. The labels represent either the main gene causing each disease or a short disease name. Please note that the DMD class (dystrophinopathies) includes both Duchenne and Becker muscular dystrophies.

2.2 | Muscle Score Harmonization

To merge existing datasets with different muscle groupings, we defined two simple operations: muscle merging and group expansion. Muscle merging joins multiple muscles into a single muscle group by averaging the scores of each individual muscle (*peroneus brevis* and *peroneus longus* into *peronei*). Group expansion divides a muscle group into its individual muscles by assigning the same score to each muscle (*biceps femoris* into *biceps femoris long head* and *biceps femoris short head*).

We averaged bilateral scores into mean muscle scores. The asymmetry of each muscle was defined as the difference between both sides, and the mean and standard deviation of the asymmetry were calculated for each patient.

We normalized all scales to a range between 0 (*healthy muscle*) and 100 (*completely fat-replaced muscle*), considering the range of values of each original scale. Fat fraction scores were not normalized, as they already range between 0 and 100. Then, we rescaled the scores by subtracting the leave-one-out mean of each patient from each muscle fat replacement feature. This transformation removes the information representing the overall amount fatty replacement, which indicates the disease stage of the patient. To keep this crucial information, we added the mean muscle involvement of each patient (before scaling the scores into relative scores) as an additional feature. After processing, fat score features are left in a range between –100 and 100. Negative values indicate muscles with a lower fat content than the average of the patient, and vice versa.

2.3 | Missing Data

The final dataset consists of an aggregate of patient data from various sources and studies, collected following distinct protocols. The muscles reported by different sources vary, leading to blocks of missing information for some disorders. We imputed missing values using the K-nearest neighbour (KNN) algorithm, which has proven to perform well with blocks of missing data, as it does not make strong assumptions about the distribution of the data, leverages information from complete features and captures multivariate relationships [S25, S26].

2.4 | Oversampling and Data Augmentation

To mitigate the impact of class imbalance, the Synthetic Minority Oversampling Technique for Nominal and Continuous (SMOTE-NC) was employed [S27]. This technique involves generating synthetic samples for the minority classes, thereby increasing their representation in the dataset. SMOTE-NC helps prevent the model from being biased towards the majority class, resulting in more balanced training data.

Additionally, SMOTE-NC allows to further mitigate scale information leakage by blurring the quantization after rescaling the fat scores. We modified SMOTE-NC to oversample all classes, including the majority class, regulated by the parameter *augmentation_factor*. Resampling was performed only on the training subset to avoid leaking training information into the validation data. Hence, we use SMOTE-NC as a general data augmentation technique.

2.5 | Model Training and Evaluation

The processed data were used to train and validate an XGBoost classifier using a nested cross-validation approach. The outer cross-validation splits the data into 10 stratified folds to provide an unbiased estimate of the model's performance. Samples were

TABLE 1 | Data overview.

Disease	Label	N	Mean Age	Sex		Side			Scale				
				M	F	B	A	U	0-4	0-5	1-4	2a2b	FF
Anoctaminopathy	ANO5	116	50.06	73	41	116	0	0	90	0	26	0	0
Calpainopathy	CAPN3	139	36.16	61	74	76	18	45	54	0	66	0	19
Myotonia congenita	CLCN1	31	46.07	16	15	31	0	0	31	0	0	0	0
Dystrophinopathies	DMD	179	27.22	179	0	157	0	22	106	22	0	51	0
MD type 1	DMPK	142	45.65	84	53	142	0	0	142	0	0	0	0
FSHD type 1	DUX4	489	46.34	145	143	349	140	0	336	13	0	0	140
Dysferlinopathy	DYSF	594	38.48	284	298	238	356	0	238	0	0	0	356
LGMDR9	FKRP	112	38.17	32	44	19	46	47	55	11	0	0	46
Pompe disease	GAA	116	43.08	28	31	116	0	0	116	0	0	0	0
GNE myopathy	GNE	75	34.27	32	38	57	0	18	75	0	0	0	0
Hypokalaemic periodic paralysis	HypoPP	41	45.22	27	14	41	0	0	41	0	0	0	0
Laminopathies	LMNA	85	37.88	21	23	18	67	0	77	0	8	0	0
OPDM	OPDM	77	52.21	37	40	0	69	8	77	0	0	0	0
OPMD	PABPN1	288	62.84	130	112	184	104	0	238	0	8	0	42
McArdle disease	PYGM	67	43.76	34	32	21	46	0	21	0	0	0	46
Hyperkalaemic periodic paralysis	SCN4A	30	43.87	16	14	30	0	0	30	0	0	0	0
Spinal muscular atrophy	SMN1	71	19.24	27	16	16	0	55	16	0	0	55	0
Sarcoglycanopathies	SarcoG	170	20.98	55	51	84	64	22	84	22	64	0	0
Titinopathy	TTN	81	18.38	41	36	81	0	0	32	49	0	0	0
VCP-related myopathy	VCP	58	51.64	31	12	4	0	54	4	0	54	0	0

Note: Each disease has a shorter label assigned, which has been used throughout this document. The age column shows the mean value, whereas the rest shows the sample counts. Counts of samples with an unknown sex are not represented. Sex is coded as M (male) and F (female). The scores side is encoded as B (bilateral score), A (average scores) and U (unilateral scores). The different scales used to measure fat replacement are the 5-point Mercuri score (0–4), 6-point Mercuri score (0–5), 4-point Mercuri score (1–4), 5-point Mercuri score with two subcategories on point 2 (2a2b) and Dixon fat fraction (FF). The definition of each scale is available in Figure 1a. Abbreviations: FSHD, facioscapulohumeral muscular dystrophy; MD, myotonic dystrophy; OPDM, oculopharyngodistal myopathy; OPMD, oculopharyngeal muscular dystrophy.

grouped by patient to avoid mixing multiple samples of the same patient in different folds. The inner cross-validator splits the data into 5 stratified folds to optimize the hyperparameters.

We conducted a comparative analysis of the performance of XGBoost and random forest, the latter being another widely used decision tree-based algorithm, which we employed in our previous pilot study [18]. Additionally, we evaluated the efficacy of KNN for the classification task [19], considering that KNN was also utilized for data imputation in this study.

Given the presence of class imbalance in the dataset, the optimization was based on the balanced accuracy metric, which accounts for the unequal distribution of classes and prevents bias towards the majority class. This approach aimed to enhance the model's generalizability and its ability to accurately classify instances from all classes, including the minority ones. Balanced accuracy is defined as the average recall obtained in each class.

We also calculated a class-weighted top-n accuracy, W_n , defined as in Equation (1).

$$W_n = \frac{\sum_{i=1}^S w_{y_i} \cdot I(y_i \in P_{n,i})}{\sum_{i=1}^S w_{y_i}} \quad (1)$$

where w_{y_i} is the weight assigned to the class y of the sample i , S is the total number of samples, and I is the indicator function that returns 1 if the true label y_i is within the top n predictions $P_{n,i}$ and 0 otherwise. We calculate the class weights as the inverse of the class frequencies, expressed in Equation (2).

$$w_i = \frac{S}{\text{count}(y_i)} \quad (2)$$

where $\text{count}(y_i)$ is the number of samples belonging to the class y_i .

We also evaluated the model by calculating the One-vs-Rest and One-vs-All receiver operating curves (ROCs) and precision–recall curves (PRCs). To calculate the One-vs-Rest PRCs, the multiclass classification is decomposed into multiple binary classification problems. For each class, we calculated the ROC by treating that class as the positive class and all others combined as the negative class. This allows us to assess classifier performance for each class against the rest.

When calculating the One-vs-One PRCs, the results are again broken down into multiple binary classification problems. For each pair of diseases, the model is evaluated twice: first by considering one of the diseases as the positive class and the other as the negative class and then the other way around. The results of both are averaged to represent the PRC curve for the pair of diseases.

2.6 | Hyperparameter Optimization

We optimized the hyperparameters using Bayesian optimization techniques. Bayesian optimization works by sampling points in the parameter space using the results of previous sampled points, converging orders of magnitude faster than a grid search of parameters and yielding better results than a random parameter search [S28].

A tree-structured Parzen estimator (TPE) was used to sample points in the parameter space [S29], and each parameter combination was tested using the inner cross-validator. Hyperparameter optimization was performed using the Optuna framework [S30].

The TPE sampler was initialized with 30 points, and 60 different hyperparameter combinations were sampled at each fold. The parameter combinations with performance over the 90th percentile of each outer cross-validation fold were used to create an ensemble of XGBoost models by averaging the outputs of each individual model. Given that the SHAP values used for explaining the model are calculated using the raw marginal outputs of the XGBoost models, we averaged the marginal outputs of the ensemble and applied the softmax function to the result, defined as in Equation (3).

$$\text{softmax}(x) = \frac{e^{x_{ik} - \max(X_i)}}{\sum_{k=1}^K e^{x_{ik} - \max(X_i)}} \quad (3)$$

where X_i represents i th row of the input array X , corresponding to the set of scores for the i th instance. x_{ij} is the score for the j th class in the i th instance, and K is the total number of classes.

2.7 | AI Versus Clinical Experts' Comparison

We compared the model's performance to that of field experts using a dataset composed entirely of previously unseen mMRI scans. For each neuromuscular disorder, one scan was randomly selected. However, due to the unavailability of new mMRI scans for every disorder, this set contained 14 scans representing 14 different NMDs: FKR, DMD, VCP, DMPK, GNE, CAPN3, SCN4A, ANO5, SarcoG, DYSF, DUX4, PABPN1, LMNA and GAA.

Four clinicians with long expertise in the use of MRI for diagnosis of patients in the clinical setting participated in this experiment (C.B., G.T., V.S. and J.D.). They were blinded to the diagnosis for each scan and were told that NMDs could repeat within the test dataset. Some mMRIs included muscles not used in the model (paraspinal, arm muscles, etc.), which were manually masked out of the scans to make a fair comparison. Age and sex data were available for all patients except for patient P14, for whom the age at scan was not recorded. Most MRI scans covered the pelvis, thigh and lower leg muscles; however, patients P1 and P12 did not have lower leg images, and patients P8, P11 and P13 were missing some upper pelvic muscles.

The experts were asked to select, in order of preference, 3 potential diagnoses. They were allowed to look at the mMRI scan and use any other visual features, such as muscle morphology, intramuscular fat distribution and texture. Some experts were unable to provide the full raking for some patients due to uncertainty. These missing values were imputed by selecting a random diagnosis.

Muscles were manually scored by C. Bolaño-Díaz and processed following the pipeline defined in this manuscript. The model was used to produce predictions, and their accuracy was evaluated using top-K accuracy curves. SHAP values were used to explain each prediction, and a round table between the experts was held to evaluate the results of the experiment and gain insights about the patterns identified by the model.

3 | Results

3.1 | Harmonization and Preprocessing

Our proposed harmonization and preprocessing pipeline scales all intramuscular fat scores to a range from -100 to 100 . In this new space, negative values indicate muscles less affected than the average of the patient and vice versa. In Figure 2a,b, we show the effect of this pipeline: Before processing, scale information can be easily recovered from the muscle fat scores. Given that the distribution of scales is not equal across diseases, this information would introduce bias in the model if not accounted for. After processing, scores show a similar distribution independently of the scale and do not leak scale information into the data. A complete comparison across all target diseases can be found in Figure S1.

Scaling the fat scores by subtracting the leave-one-out mean helps in highlighting the relative involvement of muscles independently of the disease stage, allowing the identification of patterns of muscle involvement more effectively than by plotting absolute fat scores. Figure 2c shows an example of the processed data for the SarcoG class as a heatmap sorted by mean muscle fat score. We can observe an early relative involvement of the pelvic muscles (glutei, piriformis, obturators, pectineus, quadratus femoris and adductors) except for the iliopsoas and tensor fasciae latae. We can also observe a relatively low involvement of the lower leg muscles (tibialis anterior and posterior, peronei, gastrocnemii, soleus and flexors) at an intermediate disease stage. The tibialis posterior and flexor digitorum longus muscles show a minimum relative involvement at a late stage of the

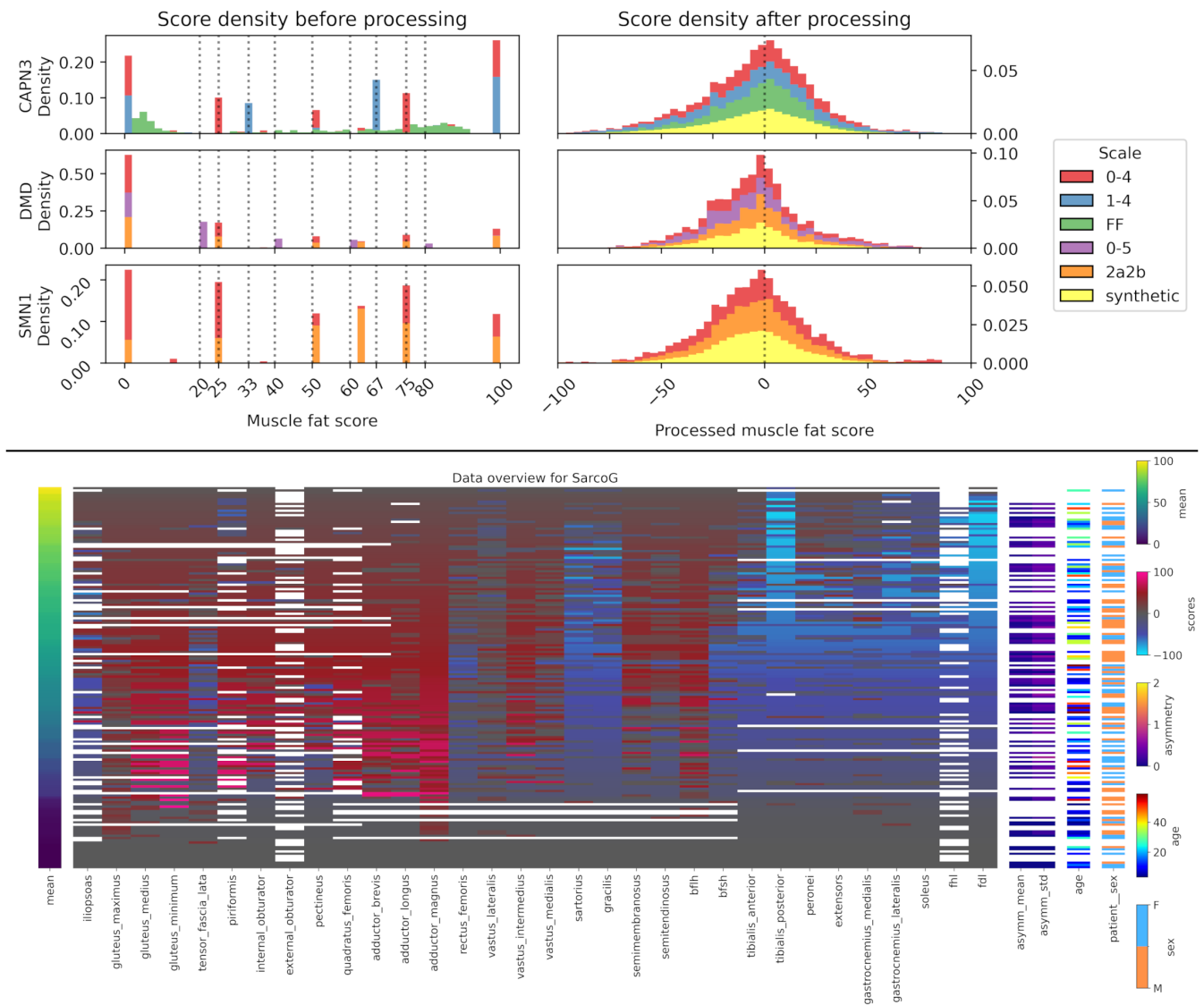


FIGURE 2 | Distribution of muscle fat scores before (a) and after (b) processing for CAPN3, DMD and SMN1. Normalized stacked densities are shown for each different scale. The discrete values shown in Figure 1a are highlighted in the left figure. Scores outside of the discretised values correspond to mean values from the left and right legs. (c) Heatmap of the data for SarcoG. Patient samples are shown in rows and features in columns. Rows are sorted by mean fat score, with late-stage patients in the upper rows and early-stage patients in the lower rows. Asymmetry is calculated as the difference between each left and right muscle, and the mean and standard deviation of the asymmetry of all muscles are added as features for each patient. Empty (white) spaces represent missing data. Muscle abbreviations: biceps femoris long head (bflh), biceps femoris short head (bfs), flexor hallucis longus (fhl) and flexor digitorum longus (fdl). The extensor digitorum longus and extensor hallucis longus have been grouped and named 'extensors'.

disease. Heatmaps for the rest of the target diseases can be found in Figures S2–S20.

3.2 | Diagnosis Model

The degree of intramuscular fat replacement, age, sex and asymmetry were used as input features to train an XGBoost classifier ensemble. The model ensemble obtained an average balanced accuracy of $64.8\% \pm 3.4\%$. We also assessed the performance of the model in suggesting multiple diagnoses by measuring the weighted top-N accuracy. This metric evaluates the percentage of samples where the ground truth is within the top-N choices of the model, weighting each class to avoid the effect

of class imbalance. We obtained a weighted top-3 accuracy of $84.7\% \pm 1.8\%$ and a weighted top-5 accuracy of $90.2\% \pm 2.4\%$.

We complemented these metrics by calculating the confusion matrix, ROC curves and PRCs of the model ensemble (Figure 3). The confusion matrix (Figure 3a) breaks down the results of the ensemble predictions by class, comparing the model predictions against the ground truth. To compensate for class imbalance and make the confusion matrix easier to interpret, we normalized it by ground truth (Figure 3b). The model ensemble predicted correctly 80% or more of the patients labelled with GNE and PABPN1 and between 70% and 80% of the patients labelled with DMPK, DUX4, DYSF, GAA and SarcoG. However, it struggled in predicting patients labelled with ANO5 and FKR, guessing

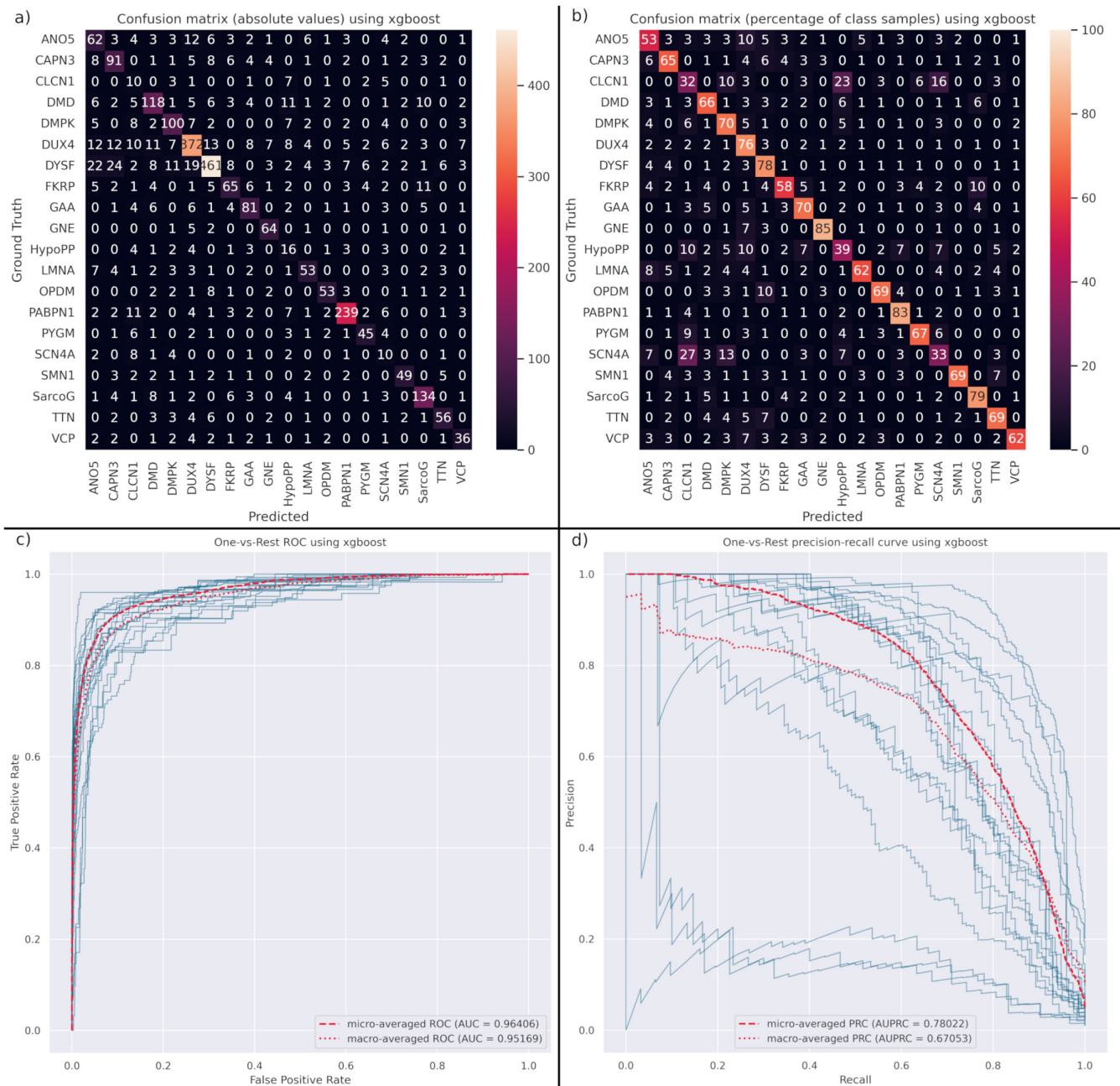


FIGURE 3 | Evaluation plots for the XGBoost model ensemble. (a) Confusion matrix of the model with the test data. The ground truth is shown in rows and the model predictions are in columns. The diagonal corresponds to the correctly predicted samples. (b) Confusion matrix normalized by ground truth (rows). (c) One-vs-Rest receiving operating curves for each disease (blue) and micro- and macro-averaged curves (red). The area under the curve for the micro- and macro-averaged curves is shown in the legend. (d) One-vs-Rest precision-recall curves for each disease (blue) and micro- and macro-averaged curves (red). The area under the precision-recall curve for the micro- and macro-averaged curves is shown in the legend.

correctly in 53% and 58% of the patients respectively. Finally, we consider that the model failed in predicting CLCN1, HypoPP and SCN4A, guessing correctly under 40% of the patients.

The latter three diseases are the least represented in the dataset (31, 41 and 30 samples respectively), and they are characterized by a mild or absent fatty replacement in muscle, except for some patients (Figure S21) [20]. This suggests that the lack of muscle involvement lowers the performance of the model in predicting these diseases, requiring additional features for providing a precise diagnosis.

The ROCs (Figure 3c) seem to offer an overoptimistic measurement of the model performance with an AUC over 0.95 for both the micro- and macro-averaged ROCs. This can be explained as an effect of class imbalance, which is better leveraged by the PRC [21]. In the One-vs-Rest PRC curves (Figure 3d), we can easily identify the three underperforming curves (corresponding to CLCN1, HypoPP and SCN4A). Still, the micro- and macro-averaged PRC curves suggest a good overall performance, with AUPRCs of 0.780 and 0.671 respectively. The performance metrics for each disease are shown in Table S1.

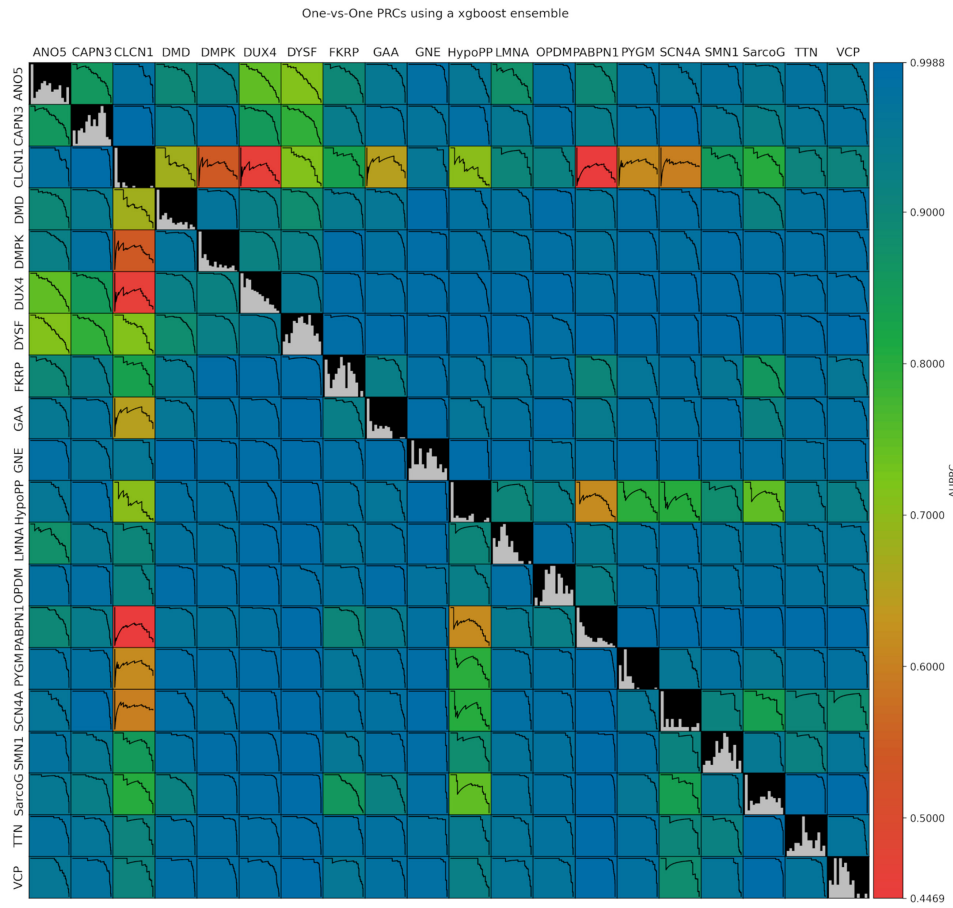


FIGURE 4 | Average One-vs-One precision–recall curves. The areas under the precision–recall curves (AUPRC) are represented for each pair of diseases. Histograms of the mean fat score for each NMD are shown in the diagonal.

To further understand the performance of the model, we calculated the One-vs-One PRCs (Figure 4). Again, we can observe a lower performance when predicting CLCN1, HypoPP and SCN4A, especially when comparing them against diseases with a high positively skewed mean fat score distribution. We also observe how the model tends to confuse ANO5 and CAPN3 with DUX4 and DYSF. The latter two are the majority classes in the data and seem to bias the model, lowering the performance in predicting ANO5 and CAPN3. The rest of the diseases do not appear to be affected by this.

3.3 | Classifier Comparison

Random forest achieved comparable results to XGBoost, obtaining a balanced accuracy of $64.3\% \pm 3.0\%$. KNN required significantly lower resources and time to train with minimal hyperparameter optimization and managed to achieve a balanced accuracy of $59.3\% \pm 2.3\%$ (Figure S22).

3.4 | Model Interpretation

The SHAP framework, grounded in the cooperative game theory concept of Shapley values, offers an intuitive and theoretically robust method for dissecting the decision-making processes of various machine learning models [22]. It achieves this

by attributing the contribution of each feature in the dataset to the model's prediction, unravelling the opaque inner workings of complex models.

Traditionally, the patterns of muscle involvement in different diseases have been described in an isolated way or within small disease groups. Although this method helps characterize the progression of a disease, patterns identified in this way lack the differential specificity to help diagnose NMD patients [14]. By using SHAP values, we can identify patterns of muscle involvement unique for each disease within the pool of NMDs used to train the diagnosis model. A more detailed explanation on SHAP and how it can be interpreted is available in the Data S2.

In Figure 5a, we show a heatmap with the mean absolute SHAP value of each feature (columns), divided by each NMD (rows). We clustered the SHAP values to identify disease groups by feature importance. The model identifies two main groups: diseases characterized by the mean fat score (PYGM, DMPK, CLCN1, OPDM and SCN4A) and diseases characterized by the gastrocnemius medialis, soleus, age and adductor magnus (PABPN1, SMN1 and SarcoG). The vastus lateralis and medialis are especially relevant in diagnosing GNE. These muscles have been described to be completely spared in early and mid-stage patients, showing involvement mostly in the final stage of the disease [23, 24].

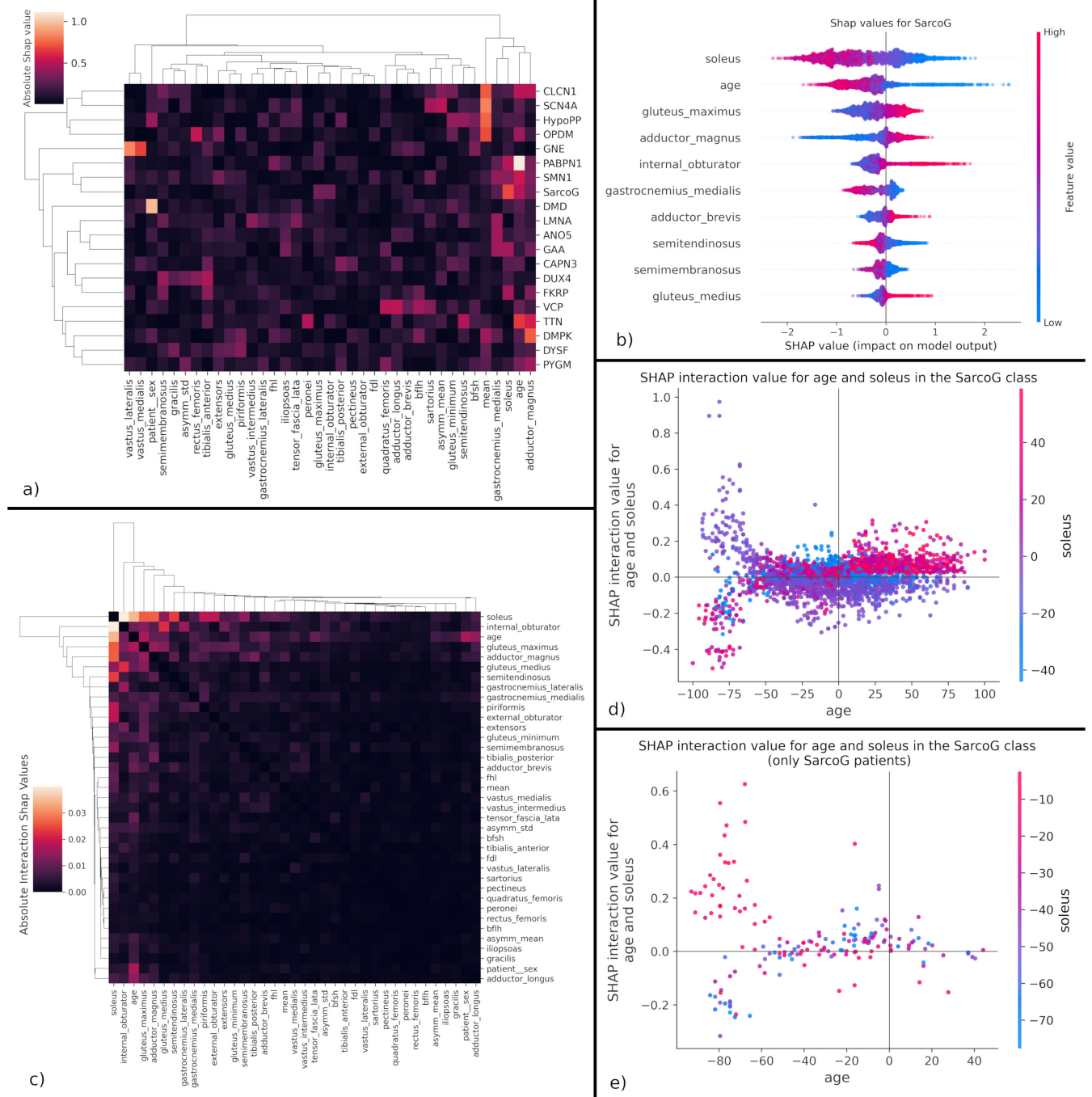


FIGURE 5 | Model explainability using SHAP values. (a) Clustered mean absolute SHAP value. Features are shown in columns and diseases are shown in rows. The absolute SHAP value gives an overall indication of the importance of each feature. (b) SHAP values of the 10 most important features in predicting SarcoG, with each patient represented as a dot. Positive SHAP values indicate a positive impact on the prediction (increase in odds of predicting the target disease) and vice versa. Feature values are colour-coded: 'High' is equivalent to the maximum feature value, and 'low' is equivalent to the minimum feature value. (c) Clustered mean absolute interaction values for SarcoG. The main effect values (diagonal) have been set to 0 to avoid obscuring the interaction values. (d) Interaction values between age and soleus for SarcoG, showing all patients. (e) Interaction values between age and soleus for SarcoG, only showing patients diagnosed with SarcoG (ground truth). Age is normalized to a -100–100 range.

We can further explore the importance of features for each disease by analysing the distribution of SHAP values within each disease and feature. Taking SarcoG as an example (Figure 5b), we can observe how having a high age is consistently associated with not having SarcoG, as indicated by the wide trail of negative shape values. In contrast, the long trail of positive SHAP

values for the age feature suggests that having a low age is extremely important for some specific patients. SHAP values for all diseases are available in Figure S23.

Understanding the interactions between features can provide deeper insights into the characteristic patterns of each disease.

SHAP allows us to calculate interaction values for each pair of features; however, analysing each pair of interactions becomes impractical as the feature space increases. To approach this problem, we proposed clustering the mean absolute interaction values. For the SarcoG example (Figure 5c), we observe how the age, gluteus maximus and soleus have larger absolute interaction values, suggesting a synergy between these features. When analysing the interaction between soleus and age (Figure 5d,e), we observe that involvement of the soleus close to the average of the patient (values close to 0) at an early age increases the odds of diagnosing SarcoG. Although the scientific community has already identified a rapid-progressing childhood variant and slow-progressing adult-onset variant for SarcoG [7, 25], we are, to the best of our knowledge, the first ones to link these variants to the soleus involvement as a discriminative feature for diagnosing SarcoG.

3.5 | AI Versus Experts' Results

In the comparative evaluation between the AI model and experienced clinicians in mMRI analysis, Myo-Guide demonstrated the highest top-3 accuracy ($75.0\% \pm 4.8\%$), outperforming Expert D (64.3%) as shown in Figure 6a. Conversely, when considering only the primary prediction, the model ranked third ($48.6\% \pm 8.9\%$), with Expert A achieving the highest accuracy (57.4%). A comprehensive breakdown of these results is provided in Figure 6b. Notably, both the model and the clinicians partially or entirely misclassified patients P1 (FKRP), P3 (VCP), P7 (SCN4A) and P13 (LMNA), suggesting that these cases exhibited atypical representations. In the case of patient P3, both the model and the experts consistently misdiagnosed the condition as GNE rather than VCP. An analysis of the SHAP values for patient P3's prediction revealed that the preservation of the

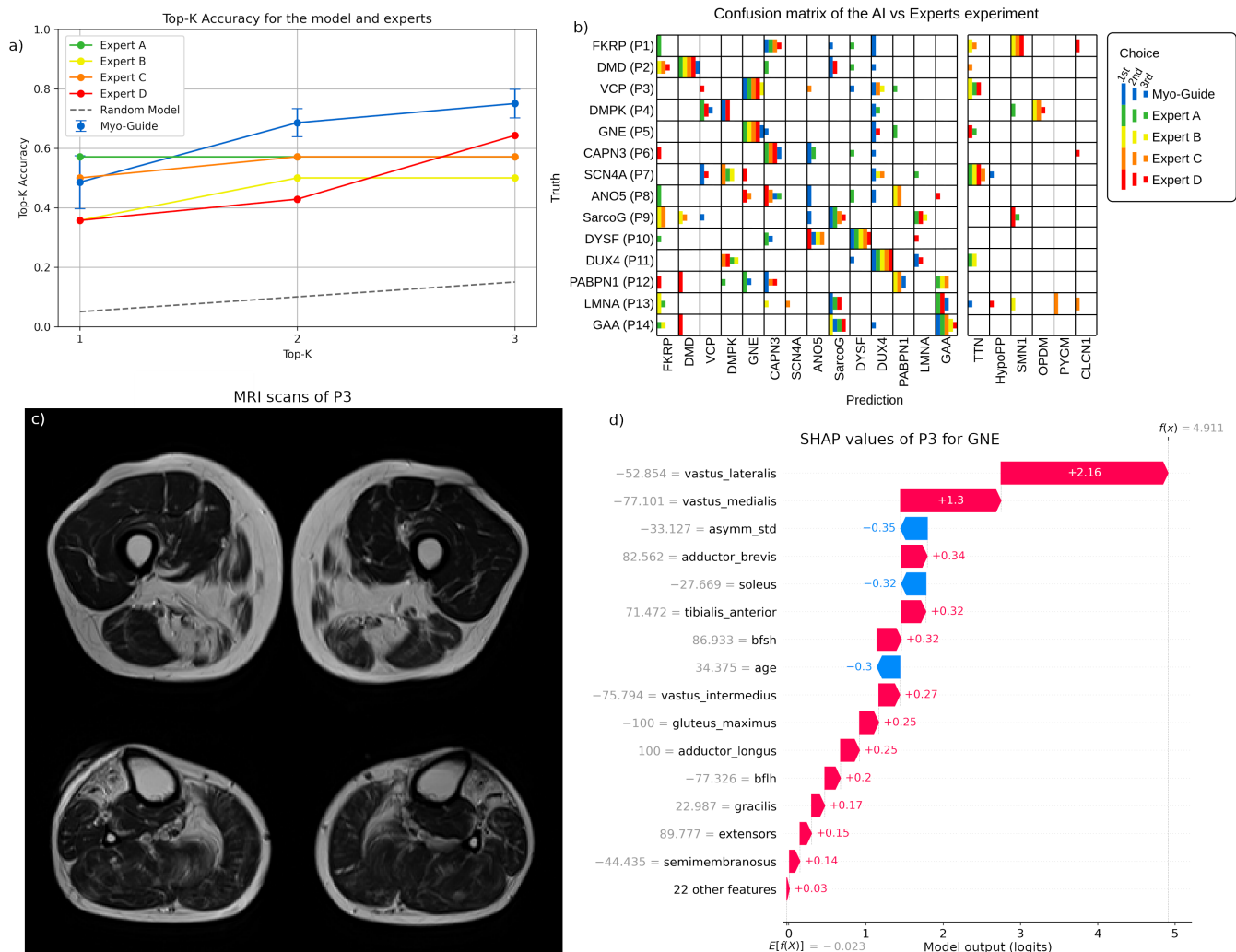


FIGURE 6 | (a) Top-K accuracy curves of the model (Myo-Guide) and experts in the final AI versus experts' experiment. Error bars are available for the model, representing the standard deviation of the model ensemble. The Top-K accuracy curve of a random classifier is also provided. (b) Confusion matrix of the AI versus experts' experiment, with each answer represented as a bar. Each expert (and model) is colour-coded, and the ranking of each choice is represented by the length of the bar. The predicted diagnoses not included in the test set (TTN, HypoPP, SMN1, OPDM, PYGM and CLCN1) are separated from the rest for visual clarity. Bars in the diagonal represent correct predictions and vice versa. (c) mMRI scan of P3 showing thigh and lower leg. (d) Waterfall plot of the SHAP values for P3 when predicting GNE. The y-axis represents the features (with values) sorted by decreasing importance (top to bottom). The x-axis represents the raw output of the model (in logits). The plot shows the impact each feature had towards the model output. Note that all feature values are scaled to a range of -100 and 100 (including age and asymmetry).

anterior thigh compartment and the involvement of the posterior compartment were the primary contributing factors to this prediction.

3.6 | Development of a Web Containing the Algorithm Described

The model has been deployed on the Myo-Guide web platform, accessible at www.myoguide.org. The platform offers an interactive user interface to use the diagnosis model (Figure S24). No identifiable information is required, and no data are stored after submitting a request. The web deployment of the model allows its integration with clinical and genetic workflows, providing clinicians and experts with additional information helpful in the diagnosis process of patients.

4 | Discussion

In this paper, we introduced a novel pipeline for processing and harmonizing multi-study muscle fat replacement data obtained using MRI for diagnostic purposes. This advancement allowed us to gather the largest dataset published to date of muscle MRI data in NMD patients, enabling a new automated approach to the diagnosis of these disorders. With that objective in mind, we proposed a scalable methodology using AI and proved its performance in diagnosing patients encompassing 20 different diseases. We also adapted well-established AI explainability techniques to explore distinctive patterns of muscle involvement, finding clues for diagnosis undescribed in previous research. Finally, we aimed to translate all these efforts into an immediate improvement in clinical practice by offering the model as a free web application.

We designed the complete pipeline to allow for different muscle fat scoring systems, with special care to quantitative measures such as the fat fraction. Radiology trends point towards an increase in the adoption of quantitative techniques, hence the importance of future-proofing current technologies [26, 27]. Recent advancements in automatic muscle segmentation [28], together with the approaches presented here, are steps towards a streamlined approach to NMD diagnosis using MRI.

This processing pipeline also helps correct the potential effect of inter-operator variability bias in qualitative scores. Scorers who tend to exaggerate fat involvement will (to some extent) score all muscles higher and vice versa. By using the mean of each patient to scale the scores, we convert the scores from an absolute measure of fat to a relative one, attenuating differences between scoring styles.

Still, there is a need for strategies enabling the reusability of retrospective data, allowing to automatically measure fat in T1w MRI scans and other imaging modalities. Different studies have proven the correlation between fat fraction and fat measurements obtained with other MRI techniques [29, 30], suggesting that such a system is possible.

In the same line as our work, Wei et al. [11] presented an AI model for differentiating necrotizing myopathy from

dysferlinopathy using a mix of radiomic features and Mercuri fat scores, obtaining AUCs over 0.9. Nagawa et al. [12] presented several radiomics-based models to classify patients diagnosed with dermatomyositis, amyopathic dermatomyositis and polymyositis, obtaining accuracies of approximately 61%. Monforte et al. [13] also presented a random forest model for differentiating between FSHD and non-FSHD patients using Mercuri fat scores from upper and lower body muscles, obtaining an accuracy of 89%. Although current studies demonstrate the increasing role of AI in diagnosing NMD patients, these are still limited to a few diseases, and there is a lack of a standardized approach. We consider the pipeline presented in this paper as a breakthrough in this context, establishing best practices for muscle fat replacement data collection and standardization, design of automated diagnosis models and critical evaluation to avoid over-optimistic performance metrics.

The applied AI explainability techniques provide an opportunity to reanalyse all the muscle fat data published during the last decades with a depth that was not possible before. Using our approach, muscle involvement can be characterized in the context of a large pool of diseases. Therefore, differential disease characteristics can be identified to aid in the diagnosis of these disorders. In the past, MRI was considered inaccurate in diagnosing some diseases, such as anoctaminopathy [31], due to the overlapping of muscle involvement patterns with other disorders [14]. Although our model has difficulties in diagnosing anoctaminopathy, we managed to predict more than half the anoctaminopathy patients correctly. Future studies should focus on applying the proposed explainability techniques to each one of the included diseases to expand our understanding of their clinical representations.

During the lifetime of this project, we observed the diagnosis model decay in performance as the number of diseases included increased. We reached a point where the addition of new samples did not necessarily translate into an improvement. Moreover, further increasing the number of samples for the majority classes might lower the performance of the model, as we demonstrated. The model could be improved by integrating more predictive features, such as upper-body muscle fat data [32], muscle inflammation data obtained with fluid-sensitive techniques such as the fat-suppressed T2w or STIR MRI sequences [33] and clinical features.

The inclusion of disorders with minimal or no fatty replacement (CLCN1, HypoPP and SCN4A) accentuated the drop in performance when compared with our 2020 study, especially when considering balanced metrics. It could be argued that a patient diagnosed with one of these disorders is, from the model's perspective, no different than a patient with a pre-symptomatic or early stage of a disorder where fatty replacement is common. Additionally, the lack of muscle involvement in patients who have muscle weakness in clinical examination has been defined as characteristic of some disorders, such as myasthenic syndromes or channelopathies [34, 35]. For these reasons, and to avoid cherry-picking, we decided to keep these disorders in the dataset. One potential solution for a future version of the model could be to group all the diseases that have a normal or near-normal MRI under the same category.

Other limitations of our approach are intrinsic to the features used for training the model. Muscle fat is not homogeneously

distributed across the muscle volume, but there are different 'textures' of fat and patterns that can be useful for diagnosis [36]: popcorn fat (or fat pockets) in VCP [15], fat ring in Bethlem disease [37] and proximo-distal distribution in sarcoglycanopathies [7], to enumerate a few. Mercuri-based scales do not capture this information, as they approximate the whole muscle fat content as a single score. Dixon sequences could alleviate this by quantifying the complete muscle volume, although complex texture information could be captured using radiomics, an image analysis modality.

Also related with the latter limitation, this study challenges some accepted ideas on the patterns of muscle involvement, such as confusing SarcoG with FKRP more than with GAA. The presented model uses exclusively the overall amount of fatty replacement, age and sex; and it has no knowledge of fat distribution/texture, muscle hypertrophy/atrophy and other characteristics easily picked up by the expert's eye. The model has also no knowledge of the patient's family history, ethnic or geographic origin of the patient and other key clinical information. This leads to interesting results that challenge the descriptive papers published so far. By blinding the model to all other predictive features usually used in diagnostics, we can isolate the muscle involvement patterns from other predictive features observed both in and out of the MRI, allowing for a comprehensive understanding of these patterns.

Increasing the number of features would introduce another problem, as the complexity of collecting, curating and harmonizing the data would significantly increase [38]. Additionally, blocks of missing values would arise in the data as not all imaging modalities or body regions would be available for all patients. This has been solved here to an extent, but more specialized techniques might be necessary if the problem increases. This is an active topic of research, and multiple methods have been proposed over the last years to solve this problem [39, 40].

The detection of patients with a disorder outside of the presented pool of diseases (outlier detection) is not addressed in this study. Although classification and outlier detection are distinct tasks, the use of model confidence could provide insights into potential outliers. However, care must be taken to distinguish between patients with rare disease sub-patterns and those with conditions not represented in the model. This remains an important area for future research, particularly in the context of neuromuscular diseases, where rare cases are common and clinically significant.

The final AI versus experts' experiment revealed not only the efficacy of the model in suggesting potential diagnoses. The concordance between the model and expert assessments in misclassified patients suggests that the AI system can identify differential patterns even in atypical cases. This information is key to ensure that the model predictions are kept grounded to clinically relevant features.

The proposed methods represent a leap forward in the way we use MRI for studying NMDs. By designing a flexible data standard and harmonization methods, we managed to conglomerate a large repository of rare disease data. This is an essential step

in this new age of data-driven approaches, which paves the way for a new wave of AI-based strategies to study muscle MRI in NMDs. The presented online tool is especially useful for clinicians and geneticist, enhancing the decision-making during the diagnosis pipeline with the outcomes of the AI-based analysis. This tool can help with patients carrying a variant of unknown significance in a specific gene or patients who have multiple pathogenic variants in several genes. In those cases, having an MRI compatible with a specific pattern can help in the diagnosis process. Future work will expand on the methods proposed here, improving the diagnostic pipeline and deepening our understanding of these conditions.

Affiliations

¹John Walton Muscular Dystrophy Research Centre, Newcastle University, Newcastle upon Tyne, UK | ²Department of Medicine (Neurology), The Ottawa Hospital, Ottawa, Canada | ³Department of Genetics, Children's Hospital of Eastern Ontario, Ottawa, Canada | ⁴Ottawa Hospital Research Institute, Ottawa, Canada | ⁵Copenhagen Neuromuscular Centre, Rigshospitalet, Copenhagen University Hospital, Copenhagen, Denmark | ⁶Department of Neurology, Huashan Hospital, Fudan University, Shanghai, China | ⁷Neuromuscular Disorders Unit, Neurology Department, Hospital 12 de Octubre, Madrid, Spain | ⁸Hospital Universitari Vall d'Hebron, Barcelona, Spain | ⁹Neuromuscular Disorders Unit, Neurology Department, Hospital Universitari Vall d'Hebron, Barcelona, Spain | ¹⁰Department of Brain and Behavioural Sciences, University of Pavia, Pavia, Italy | ¹¹Advanced Imaging and AI Center, Mondino IRCCS Foundation, Pavia, Italy | ¹²University of Pavia; Mondino IRCCS Foundation, Pavia, Italy | ¹³UOC di Neurologia, Fondazione Policlinico Universitario Agostino Gemelli IRCCS, Rome, Italy | ¹⁴Fondazione Policlinico Universitario Agostino Gemelli, Rome, Italy | ¹⁵Pediatric Neurology, Department of Woman and Child Health and Public Health, Child Health Area, Università Cattolica del Sacro Cuore, Rome, Italy | ¹⁶Hospital Clínico Universidad de Chile, Santiago de Chile, Chile | ¹⁷Programa de Doctorado en Ciencias Médicas y Especialidad, Escuela de Postgrado Facultad de Medicina Universidad de Chile, Santiago, Chile | ¹⁸University Hospital Brno, Brno, Czech Republic | ¹⁹Neuromuscular Disease Unit, Neurology Department, Hospital Universitario Nuestra Señora de Candelaria, Tenerife, Spain | ²⁰Neuromuscular Disorders Unit, Department of Neurology, Hospital de la Santa Creu i Sant Pau, Barcelona, Spain | ²¹Biomedical Research Institute Sant Pau (IIB Sant Pau), Barcelona, Spain | ²²Centro de Investigaciones Biomédicas en Red en Enfermedades Raras (CIBERER), Madrid, Spain | ²³Department of Neurology, Leiden University Medical Center, Leiden, The Netherlands | ²⁴C.J. Gorter MRI Center, Department of Radiology, Leiden University Medical Center, Leiden, The Netherlands | ²⁵Northern Care Alliance NHS Foundation Trust, Manchester, UK | ²⁶Department of Translational Research and of New Surgical and Medical Technologies, University of Pisa, Pisa, Italy | ²⁷Department of Neurology, Pusan National University School of Medicine, Busan, Republic of Korea | ²⁸Centre de Référence des Maladies du Motoneurone, Department of Neurology, Montpellier University Hospital, Montpellier, France | ²⁹Department of Neuroradiology, I2FH Platform, Montpellier University Hospital, Montpellier, France | ³⁰Leeds Teaching Hospitals NHS Trust, Leeds, UK | ³¹Paris Est University, APHP Henri-Mondor University Hospital, Créteil, France | ³²Dubowitz Neuromuscular Centre, UCL Great Ormond Street Institute of Child Health & Great Ormond Street Hospital, London, UK | ³³Department of Neuroradiology, Great Ormond Street Hospital for Children NHS Foundation Trust, London, UK | ³⁴Department of Neurology, Faculdade de Medicina da Universidade de São Paulo (FMUSP), São Paulo, Brazil | ³⁵St George's University and St George's University

Hospitals NHS Foundation Trust, London, UK | ³⁶Reference Center for Neuromuscular Disorders CHU La Timone, Aix-Marseille University, Marseille, France | ³⁷Aix-Marseille University, CRMBM, CNRS UMR 7339, Marseille, France | ³⁸Department of Neuroscience, Mental Health and Sensory Organs (NESMOS), SAPIENZA University of Rome, Rome, Italy | ³⁹Neuromuscular and Rare Disease Centre, Neurology Unit, Sant'Andrea Hospital, Rome, Italy | ⁴⁰Neuromuscular Reference Center, Department of Neurology, Universitair Ziekenhuis van Antwerpen, Universiteit Antwerpen, Antwerp, Belgium | ⁴¹University Hospital Raymond-Poincaré, Garches, France | ⁴²Neurology Department, Shariati Hospital, Neuromuscular Research Center, Tehran University of Medical Sciences, Tehran, Iran | ⁴³National Institute of Mental Health and Neurosciences (NIMHANS), Bengaluru, India | ⁴⁴Translational and Clinical Research Institute, Newcastle University, Newcastle upon Tyne, UK | ⁴⁵Interdisciplinary Computing and Complex BioSystems (ICOS) Research Group, School of Computing, Newcastle University, Newcastle upon Tyne, UK

Acknowledgements

The authors express their gratitude to the Jain Foundation and Jain COS consortium for granting access to its data repository of dysferlinopathy patients. This work has been possible thanks to all the data provided by the Myo-Guide Consortium. All members of the Consortium are listed in the [Supporting Information](#). Jose Verdu-Diaz, Carla Bolano-Diaz, Alejandro Gonzalez-Chamorro, Sam Fitzsimmons, Jaume Bacardit and Jordi Diaz-Manera disclose support for the research of this work from Muscular Dystrophy UK (grant number: 22GRO-PG24-0575 and 24GRO-PG24-0736-1) and AFM-Telethon (grant number: 23444). Jose Verdu-Diaz is also supported by the NHIR Newcastle Biomedical Research Centre (BRC) (grant number: NIHR203309). The NHIR Newcastle BRC is a partnership between Newcastle Hospitals NHS Foundation Trust and Newcastle University, funded by the National Institute for Health and Care Research (NIHR). The views expressed are those of the authors and not necessarily those of the NIHR or the Department of Health and Social Care.

Ethics Statement

The authors affirm that this manuscript conforms to the journal guidelines for ethical publication.

Conflicts of Interest

The authors declare no conflicts of interest.

Data Availability Statement

The corresponding author can facilitate a list of the publications with data included in this work. Unpublished data are not eligible for sharing due to a lack of consent from patients. Most of the dysferlinopathy data belong to the Jain COS project, available at www.jain-foundation.org. The code used for this project is published under the myoguide-diagnose python package, available at www.github.com/MYO-Guide/myoguide-diagnose.

References

1. E. Mercuri and F. Muntoni, "Muscular Dystrophies," *Lancet* 381, no. 9869 (2013): 845–860.
2. C. Nuñez-Peralta, J. Alonso-Pérez, and J. Díaz-Manera, "The Increasing Role of Muscle MRI to Monitor Changes Over Time in Untreated and Treated Muscle Diseases," *Current Opinion in Neurology* 33, no. 5 (2020): 611–620.
3. J. R. Dahlqvist, P. Widholm, O. D. Leinhard, and J. Vissing, "MRI in Neuromuscular Diseases: An Emerging Diagnostic Tool and Biomarker for Prognosis and Efficacy," *Annals of Neurology* 88, no. 4 (2020): 669–681.
4. J. Burakiewicz, C. D. J. Sinclair, D. Fischer, G. A. Walter, H. E. Kan, and K. G. Hollingsworth, "Quantifying Fat Replacement of Muscle by Quantitative MRI in Muscular Dystrophy," *Journal of Neurology* 264, no. 10 (2017): 2053–2067.
5. P. Pezeshk, A. Alian, and A. Chhabra, "Role of Chemical Shift and Dixon Based Techniques in Musculoskeletal MR Imaging," *European Journal of Radiology* 94 (2017): 93–100.
6. E. Mercuri, B. Talim, B. Moghadaszadeh, et al., "Clinical and Imaging Findings in Six Cases of Congenital Muscular Dystrophy With Rigid Spine Syndrome Linked to Chromosome 1p (RSM1)," *Neuromuscular Disorders* 12, no. 7 (2002): 631–638.
7. G. Tasca, M. Monforte, J. Díaz-Manera, et al., "MRI in Sarcoglycanopathies: A Large International Cohort Study," *Journal of Neurology, Neurosurgery, and Psychiatry* 89, no. 1 (2018): 72–77.
8. E. Bugiardini, J. M. Morrow, S. Shah, et al., "The Diagnostic Value of MRI Pattern Recognition in Distal Myopathies," *Frontiers in Neurology* 9 (2018): 456.
9. J. Díaz-Manera, J. Llauger, E. Gallardo, and I. Illa, "Muscle MRI in Muscular Dystrophies," *Acta Myologica* 34, no. 2–3 (2015): 95.
10. P. G. Carlier and H. Reynoudt, "The Expanding Role of MRI in Neuromuscular Disorders," *Nature Reviews. Neurology* 16, no. 6 (2020): 301–302.
11. P. Wei, H. Zhong, Q. Xie, et al., "Machine Learning-Based Radiomics to Differentiate Immune-Mediated Necrotizing Myopathy From Limb-Girdle Muscular Dystrophy R2 Using MRI," *Frontiers in Neurology* 14 (2023): 1251025.
12. K. Nagawa, M. Suzuki, Y. Yamamoto, et al., "Texture Analysis of Muscle MRI: Machine Learning-Based Classifications in Idiopathic Inflammatory Myopathies," *Scientific Reports* 11, no. 1 (2021): 9821.
13. M. Monforte, S. Bortolani, E. Torchia, et al., "Diagnostic Magnetic Resonance Imaging Biomarkers for Facioscapulohumeral Muscular Dystrophy Identified by Machine Learning," *Journal of Neurology* 269, no. 4 (2022): 2055–2063.
14. C. Bolano-Diaz, J. Verdú-Díaz, A. Gonzalez-Chamorro, et al., "Magnetic Resonance Imaging-Based Criteria to Differentiate Dysferlinopathy From Other Genetic Muscle Diseases," *Neuromuscular Disorders* 34 (2024): 54–60.
15. J. Verdú-Díaz, J. Alonso-Pérez, C. Nuñez-Peralta, et al., "Accuracy of a Machine Learning Muscle MRI-Based Tool for the Diagnosis of Muscular Dystrophies," *Neurology* 94, no. 10 (2020): e1094–e1102.
16. D. Esteller, M. Schiava, J. Verdú-Díaz, et al., "Analysis of Muscle Magnetic Resonance Imaging of a Large Cohort of Patient With VCP-Mediated Disease Reveals Characteristic Features Useful for Diagnosis," *Journal of Neurology* 270, no. 12 (2023): 5849–5865.
17. J. Warman Chardon, J. Díaz-Manera, G. Tasca, et al., "MYO-MRI Diagnostic Protocols in Genetic Myopathies," *Neuromuscular Disorders* 29, no. 11 (2019): 827–841.
18. L. Breiman, "Random Forests," *Machine Learning* 45, no. 1 (2001): 5–32.
19. J. Laaksonen and E. Oja, "Classification With Learning k-Nearest Neighbors," in *Proceedings of International Conference on Neural Networks (ICNN'96)*, (1996): 1480–1483.
20. L. N. Jacobsen, M. G. Stemmerik, S. V. Skriver, J. J. Pedersen, N. Løken, and J. Vissing, "Contractile Properties and Magnetic Resonance Imaging-Assessed fat Replacement of Muscles in Myotonia Congenita," *European Journal of Neurology* 31, no. 4 (2024): e16207.
21. P. Branco, L. Torgo, and R. P. Ribeiro, "A Survey of Predictive Modeling on Imbalanced Domains," *ACM Computing Surveys* 49, no. 2 (2016): 1–50.
22. S. M. Lundberg, G. Erion, H. Chen, et al., "From Local Explanations to Global Understanding With Explainable AI for Trees," *Nature Machine Intelligence* 2, no. 1 (2020): 56–67.

23. C.-Y. Liu, J. Yao, W. C. Kovacs, et al., "Skeletal Muscle Magnetic Resonance Biomarkers in GNE Myopathy," *Neurology* 96, no. 5 (2021): e798–e808.
24. G. Tasca, E. Ricci, M. Monforte, et al., "Muscle Imaging Findings in GNE Myopathy," *Journal of Neurology* 259, no. 7 (2012): 1358–1365.
25. C. Angelini, M. Fanin, M. P. Freda, D. J. Duggan, G. Siciliano, and E. P. Hoffman, "The Clinical Spectrum of Sarcoglycanopathies," *Neurology* 52, no. 1 (1999): 176.
26. P. Widholm, A. Ahlgren, M. Karlsson, et al., "Quantitative Muscle Analysis in Facioscapulohumeral Muscular Dystrophy Using Whole-Body Fat-Referenced MRI: Protocol Development, Multicenter Feasibility, and Repeatability," *Muscle & Nerve* 66, no. 2 (2022): 183–192.
27. K. Engelke, O. Chaudry, L. Gast, et al., "Magnetic Resonance Imaging Techniques for the Quantitative Analysis of Skeletal Muscle: State of the Art," *Journal of Orthopaedic Translation* 42 (2023): 57–72.
28. A. Agosti, E. Shaqiri, M. Paoletti, et al., "Deep Learning for Automatic Segmentation of Thigh and Leg Muscles," *Magma* 35, no. 3 (2022): 467–483.
29. P. F. Felisaz, G. Colelli, E. Ballante, et al., "Texture Analysis and Machine Learning to Predict Water T2 and Fat Fraction From Non-Quantitative MRI of Thigh Muscles in Facioscapulohumeral Muscular Dystrophy," *European Journal of Radiology* 134 (2021): 109460.
30. P. Trueb, J. M. Getzmann, E. Ried, E. Deininger-Czermak, H. I. Garcia Schueler, and R. Guggenberger, "Comparison of Muscle fat Fraction Measurements in the Lower Spine Musculature With Non-Contrast-Enhanced CT and Different MR Imaging Sequences," *European Journal of Radiology* 150 (2022): 110260.
31. A. Sarkozy, M. Deschauer, R. Y. Carlier, et al., "Muscle MRI Findings in Limb Girdle Muscular Dystrophy Type 2L," *Neuromuscular Disorders* 22 (2012): S122–S129.
32. J. Ropars, F. Gravot, D. Ben Salem, F. Rousseau, S. Brochard, and C. Pons, "Muscle MRI: A Biomarker of Disease Severity in Duchenne Muscular Dystrophy? A Systematic Review," *Neurology* 94, no. 3 (2020): 117–133.
33. S. Nicolau and E. Naddaf, "Muscle MRI for Neuromuscular Disorders Using Muscle MRI to Diagnose Neuromuscular Conditions Requires Awareness of Different Patterns of Muscle Involvement," (2020).
34. V. Vivekanandam, K. Suetterlin, E. Matthews, et al., "Muscle MRI in Periodic Paralysis Shows Myopathy Is Common and Correlates With Intramuscular Fat Accumulation," *Muscle & Nerve* 68, no. 4 (2023): 439–450.
35. S. Finlayson, J. M. Morrow, P. M. Rodriguez Cruz, et al., "Muscle Magnetic Resonance Imaging in Congenital Myasthenic Syndromes," *Muscle & Nerve* 54, no. 2 (2016): 211–219.
36. G. Tasca, M. Monforte, C. De Fino, R. A. Kley, E. Ricci, and M. Mirabella, "Magnetic Resonance Imaging Pattern Recognition in Sporadic Inclusion-Body Myositis," *Muscle & Nerve* 52, no. 6 (2015): 956–962.
37. E. Mercuri, A. Lampe, J. Allsop, et al., "Muscle MRI in Ullrich Congenital Muscular Dystrophy and Bethlem Myopathy," *Neuromuscular Disorders* 15, no. 4 (2005): 303–310.
38. S. Tarazona, A. Arzalluz-Luque, and A. Conesa, "Undisclosed, Unmet and Neglected Challenges in Multi-Omics Studies," *Nature Computational Science* 1, no. 6 (2021): 395–402.
39. G. Yu, Q. Li, D. Shen, and Y. Liu, "Optimal Sparse Linear Prediction for Block-Missing Multi-Modality Data Without Imputation," *Journal of the American Statistical Association* 115, no. 531 (2020): 1406–1419.
40. Y. Zhang, N. Tang, and A. Qu, "Imputed Factor Regression for High-Dimensional Block-Wise Missing Data," *Statistica Sinica* 30, no. 2 (2020): 631–651.

Supporting Information

Additional supporting information can be found online in the Supporting Information section.